Dalton Transactions

ROYAL SOCIETY OF CHEMISTRY

PAPER

View Article Online
View Journal | View Issue

Cite this: *Dalton Trans.*, 2025, **54**, 16014

$RCuMg_2$ compounds (R = Dy–Tm, Lu): crystal structure, chemical bonding and magnetic properties

P. Solokha, [a] D. Skachko, [b] R. Freccero, [a] J. Kortus, [c] R. Gumeniuk [b] and S. De Negri *[a]

The $RCuMg_2$ intermetallics (R = Dy–Tm, Lu) were found to crystallize in a new structure type ($DyCuMg_2$, *oP*32, space group: *Pmma*, a = 13.5397(4), b = 3.7594(1), c = 13.7985(4) Å). This unique crystal space is characterized by the presence of clusters formed by four Cu-centred trigonal prisms sharing edges to create a cubic-like cavity occupied by a Mg atom; 2D wavy slabs of these star-like fragments and of Mg with a *bcc* topology are alternated along the *c*-direction. An architecture based on similar moieties was recognized for the related R_2Cu_2Mg (*tP*10-Mo_2FeB_2) and $RCuMg_4$ (*oS*48-$TbCuMg_4$) compounds, proposing a generalization scheme. Electronic structure calculations and a chemical bonding analysis in the position space were applied to $LuCuMg_2$, as a representative. The calculated effective charges indicated that Lu and Cu act as the QTAIM cation and anion, respectively, and the Mg species show a slight positive charge, except that at the centre of the *bcc*-fragment, showing a tiny negative one. In general, a complex bonding scenario was revealed, dominated by both hetero and homoatomic (within the Mg *bcc*-slabs) multicentre interactions. The temperature and field dependencies of magnetic susceptibility and specific heat capacity were measured for $RCuMg_2$. The nonmagnetic $LuCuMg_2$ phonon reference compound was identified as a Pauli paramagnet. The {Ho, Er, Tm}$CuMg_2$ compounds ordered antiferromagnetically at critical temperatures between about 5 and 8 K, whereas $DyCuMg_2$ revealed multiple magnetic transitions. The complexity of the magnetic behaviour of the studied compounds was indicated by the temperature evolution of magnetic entropy.

Received 11th July 2025,
Accepted 28th September 2025

DOI: 10.1039/d5dt01632k

rsc.li/dalton

1. Introduction

The R–T–Mg alloy systems (R = rare earth metal; T = transition metal) are very rich in ternary intermetallic compounds, covering different stoichiometries and crystal structures[1,2] and representing a wide range of materials for different functional and structural applications.[3–9]

Such compounds can be classified in various families, some of which have been the object of long-lasting investigations of our research group.[10–14] Here, we focus our attention on phases characterized by a 1/1 stoichiometric ratio of the R and T components; the Cu-containing ones are shown in Fig. 1 in a Gibbs triangle.

The Mg-poorest representatives correspond to the very common 2:2:1 and 1:1:1 stoichiometries and crystallize in the two ubiquitous Mo_2FeB_2 and ZrNiAl prototypes.[2] The former exists for the entire series of R elements, and the latter is limited to light rare earth metals and yttrium. At Mg contents between about 40 and 70 at%, only a few compounds have been reported: $R_5Cu_5Mg_8$, $R_5Cu_5Mg_{13}$ and $R_5Cu_5Mg_{16}$ are only known for Y, all being own prototypes,[15] and $RCuMg_4$ exists with two different structures, $UCoAl_4$-type for R = La and $TbCuMg_4$-type for R = Y, Tb–Tm.[15–17]

The Mg-richest region is the field of existence of a special class of compounds named "long-period stacking ordered (LPSO) phases" after their structural peculiarities. Despite the most studied LPSO phases contain Ni and/or Zn, some studies have been conducted even on Cu analogues, which are located in the region between ~80 and 92 at% Mg.[18–20] In our recent study on Y–Ni–Mg LPSO phases,[21] their range of existence was extended down to ~58 at% Mg; therefore, a similar situation is also not ruled out for Cu-containing systems.

The intermetallic R–Cu–Mg compounds exhibit a variety of magnetic behaviours, including ferromagnetism, antiferro-

[a]*Dipartimento di Chimica e Chimica Industriale, Università degli Studi di Genova, via Dodecaneso 31, 16146 Genova, Italy. E-mail: serena.denegri@unige.it*
[b]*Institut für Experimentelle Physik TU Bergakademie Freiberg, Leipziger Str. 23, 09599 Freiberg, Germany*
[c]*Institut für Theoretische Physik TU Bergakademie Freiberg, Leipziger Str. 23, 09599 Freiberg, Germany*

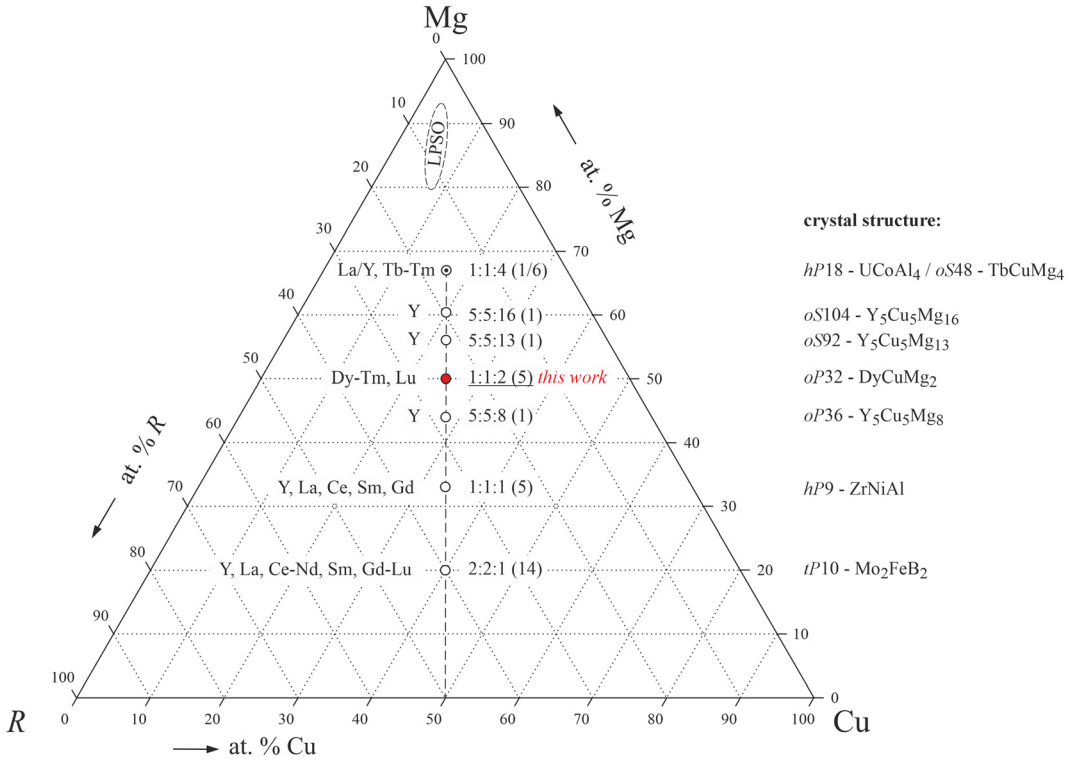

Fig. 1 Distribution and crystal structures of *R*–Cu–Mg compounds existing along the compositional line with a *R*/Cu ratio equal to 1/1. The number of representatives is indicated in parentheses. The region of existence of long-period stacking ordered (LPSO) phases known so far is also shown.

magnetism, mixed or intermediate valence states, and spin fluctuations.[1,3,22,23] For example, $\{La,Y\}_2Cu_2Mg$ were found to be Pauli paramagnets, whereas Nd_2Cu_2Mg and Pr_2Cu_2Mg ordered ferromagnetically at Curie temperatures of 42 K and 12 K, showing 3.47μ_B and 3.67μ_B magnetic moments, respectively. Interestingly, the Pr_2Cu_2Mg compound revealed an additional magnetic transition when applying an external field of ~2.5 T.[23] In contrast, Ce_2Cu_2Mg was reported to order antiferromagnetically at T_N = 7.5 K with an effective magnetic moment of 2.58μ_B, in agreement with the trivalent state of cerium ions.[22] The increase in the magnetization with the application of an external field up to $H \approx 4$ T indicated spin reorientation in this compound. Importantly, it was found that the reported magnetization of ≈0.9μ_B at 5 K and 8 T was considerably smaller than the expected moment of 2.14μ_B for fully saturated Ce^{3+}, revealing the splitting of the six fold degenerate $^2F_{5/2}$ ground state of the Ce^{3+} ion due to the crystal electric field.[22] Among the RCu_4Mg Laves phases, $TmCu_4Mg$ is paramagnetic in the entire temperature range, whereas $SmCu_4Mg$ Van Vleck's paramagnetism down to T_N = 10.8(5) K with an experimental magnetic moment of 0.69(1)μ_B has been reported.[3] Moreover, $GdCu_4Mg$ as well as $TbCu_4Mg$ undergo antiferromagnetic transitions at 48 K and 30 K, respectively, together with magnetic moments close to those of trivalent *R*-ions.[3] The recently studied orthorhombic $DyCuMg_4$ and $ErCuMg_4$ revealed two subsequent antiferromagnetic transitions at T_N = 21 and 7.9 K as well as a single ordering at T_N = 8.6 K, respectively.[17]

In this work, the results of a combined investigation on the structural and magnetic properties of the new $RCuMg_2$ series of compounds are further complemented with a chemical bonding analysis of $LuCuMg_2$, which shows a complex bonding scenario.

2. Experimental section

2.1. Synthesis and SEM/EDXS characterization

Alloys with the nominal composition $R_{25}Cu_{25}Mg_{50}$ (*R* = trivalent rare earth metal) and a total mass of about 0.6 g were prepared by direct synthesis. The pure (>99.9 mass%) metals were weighed in stoichiometric amounts, placed in tantalum crucibles, subsequently sealed by arc welding to avoid Mg loss, and induction-melted under an Ar stream. Melting was repeated three times to ensure homogeneity; then, the furnace was switched off, and the samples were left to cool down to room temperature. Subsequently, crucibles containing the as-cast samples were closed in evacuated silica ampules, annealed for 1 month at 500 °C in a resistance furnace, and then water-quenched. The samples were extracted from the crucible as partially fragmented/powdered, having the look of grey brittle alloys, stable in air for months.

Selected fragments of each alloy were embedded in two-component cold-cast Technovit epoxy resin (ATM GmbH, Germany). Surfaces suitable for metallographic analysis were obtained using the automatic polishing machine Saphir 520

(ATM GmbH, Germany); grinding with SiC abrasive papers and no lubricant was followed by polishing with 6–1 μm size diamond pastes using petroleum ether as a lubricant. Metallographic specimens were made conductive using a thin layer of graphite. A Zeiss Evo 40 scanning electron microscope (SEM) equipped with a dispersive X-ray spectroscopy (EDXS) system (INCA X-ACT) operated by the INCA Energy software (Oxford Instruments, Analytical Ltd, Bucks, U.K.) was used for microstructural analysis and compositional evaluation. The composition of each phase was established as the average of at least five measurements from different points/areas. Quantitative results agreed with the expected compositions within ~2 at% tolerance. The SEM/EDXS characterization highlighted the existence of new compounds with the $R_{25}Cu_{25}Mg_{50}$ composition in samples with R = Dy, Ho, Er, Tm, and Lu, and they became the object of this work.

2.2. XRD characterization

A good-quality $DyCuMg_2$ single crystal, selected from the mechanically crushed alloy, was glued to a glass fibre and mounted on a goniometric head. X-ray diffraction was performed on a three-circle Bruker D8 QUEST diffractometer fitted with a PHOTON III 14 photon-counting detector. The graphite-monochromatized Mo Kα radiation was used. The applied data collection strategy, elaborated using the APEX5 software,[24] consisted of four ω-scans and covered the reciprocal space up to a maximum θ of about 31° (resolution of *ca.* 0.7 Å) with exposures of 5 s per frame. Data reduction was performed using software SAINT[25] and XPREP;[26] Lorentz, polarization and absorption effects were corrected by SADABS.[27] The crystal structure was solved and refined with the aid of SHELXTL.[28] The crystal possessed orthorhombic symmetry, and the lattice parameter b (~3.76 Å) was significantly smaller than a and c (>13 Å). The best structural model was found using the intrinsic phasing method in the *Pmma* space group (N. 51), representing its own prototype. The unit cell contained 8 formula units with the $DyCuMg_2$ composition, corresponding to 32 atoms distributed among 10 Wyckoff sites (3 occupied by Dy, 2 by Cu and 5 by Mg atoms). The occupancy of each site was probed to vary, and any hint of a statistical mixture was observed so that the structural model was perfectly stoichiometric. The final anisotropic full-matrix least-squares refinement converged to excellent residuals and a flat difference Fourier map. The anisotropic displacement parameters (ADPs) of all the atoms showed a smooth distribution.

Details of data collection and structure refinement are summarized in Table 1, together with selected crystal data; standardized atomic coordinates, site occupancy factors and ADPs are listed in Table 2. The corresponding CIF file, available as SI, was deposited at the Cambridge Database.

No single crystals suitable for structure solution were found in samples with other rare earth components. For all of them, X-ray powder diffraction (XRPD) patterns were recorded on a Rigaku Smartlab diffractometer equipped with a Dtex strip detector operated in the Bragg–Brentano mode (Cu K_α radiation, continuous mode of scanning). The PowderCell[29] and CrystalDiffract[30] software were used for indexation; the precise lattice parameters of the compounds of interest were calculated by a least square routine.[31] Rietveld refinements were carried out using Fullprof software;[32] refined atomic positions for the studied compounds are available in the SI.

Table 1 Selected crystallographic data and structure refinement parameters for the $DyCuMg_2$ single crystal

Formula	$DyCuMg_2$
EDXS composition	$Dy_{23.8}Cu_{23.4}Mg_{52.8}$
Depositing CSD-code	2381656
Formula weight (g mol^{-1})	274.66
Space group	*Pmma* (N.51)
Pearson symbol-prototype, Z	*oP*32-$DyCuMg_2$, 8
a, Å	13.5397(4)
b, Å	3.7594(1)
c, Å	13.7985(4)
V, Å^3	702.36(3)
Calc. density (g cm^{-3})	5.195
Absorption coefficient (μ, mm^{-1})	27.23
Theta range (°)	$2.3 \le \theta \le 30.46$
Index ranges h, k, l	$-19 \le h \le 19$ $-5 \le k \le 5$ $-19 \le l \le 19$
Data/parameters	1259/53
GOF	1.18
R_{int}/R_{sym}	0.0311/0.015
R_1/wR_2 ($I > 2\sigma(I)$)	0.0201/0.0435
R_1/wR_2 (all data)	0.0232/0.0448
Max diff. peak and hole (e$^-$ Å^{-3})	1.023 and −1.689

2.3. Physical property measurements and computational details

The temperature and field dependencies of magnetic susceptibility and specific heat capacity were measured using a vibrating sample magnetometer (VSM) and the specific heat options of DynaCool-12 from Quantum Design, respectively.

Density functional theory (DFT) calculations to determine the electronic band structure and the relative stability of different magnetic phases were performed for $DyCuMg_2$, $HoCuMg_2$, and $ErCuMg_2$ using the linear augmented plane wave (LAPW) method, as implemented in the WIEN2K package.[33] The basis set consisted of spherical harmonics within non-overlapping muffin-tin spheres around the atoms augmented by plane waves in the space outside the muffin-tin spheres and local orbitals for the semi-core states. The core electrons were treated separately by numerically solving the radial Dirac equation in the spherical symmetric part of the potential. The kinetic energy cut-off for the plane-wave basis functions was adjusted using the product of the smallest muffin-tin radius and the largest plane-wave vector and was set here to 7. The PBESOL exchange–correlation functional[34] was applied in all calculations. The magnetism was accounted for using spin-dependent electron density in a scalar relativistic approximation for the valence and semi-core electrons.

To save computational time, all symmetry elements were kept. For the ferromagnetic state, the starting densities were created with spin-up for all the rare earth ions. In contrast, the antiferromagnetic state can only be approximated in DFT by a

Table 2 Standardized atomic coordinates and equivalent ($U_{eq.}$) and anisotropic (U_{ij}) displacement parameters for the $DyCuMg_2$ single crystal; $U_{12} = U_{23} = 0$

		Atomic coordinates			
Atom	Site	x/a	y/b	z/c	$U_{eq.}$ [Å^2]
Dy1	4*j*	0.04785(2)	$\frac{1}{2}$	0.37604(2)	0.0130(1)
Dy2	2*f*	$\frac{1}{4}$	$\frac{1}{2}$	0.18284(3)	0.0151(1)
Dy3	2*f*	$\frac{1}{4}$	$\frac{1}{2}$	0.57710(3)	0.0162(1)
Cu1	4*i*	0.09222(5)	0	0.53356(5)	0.0145(1)
Cu2	4*i*	0.09149(6)	0	0.21873(5)	0.0163(1)
Mg1	4*j*	0.5098(2)	$\frac{1}{2}$	0.1226(2)	0.0181(4)
Mg2	2*e*	$\frac{1}{4}$	0	0.3788(2)	0.0155(5)
Mg3	4*i*	0.6245(2)	0	0.2619(2)	0.0186(4)
Mg4	4*i*	0.1338(2)	0	0.0138(2)	0.0194(4)
Mg5	2*f*	$\frac{1}{4}$	$\frac{1}{2}$	0.8699(2)	0.0211(6)
Atom	Site	U_{11} [Å^2]	U_{22} [Å^2]	U_{33} [Å^2]	U_{13} [Å^2]
Dy1	4*j*	0.01466(12)	0.01320(12)	0.01116(12)	−0.00052(9)
Dy2	2*f*	0.01411(18)	0.01440(18)	0.01678(18)	0.00000
Dy3	2*f*	0.01630(19)	0.01507(18)	0.01720(18)	0.00000
Cu1	4*i*	0.0128(3)	0.0176(3)	0.0132(3)	0.0008(2)
Cu2	4*i*	0.0164(3)	0.0181(3)	0.0145(3)	−0.0016(3)
Mg1	4*j*	0.0174(9)	0.0208(10)	0.0160(9)	0.0012(8)
Mg2	2*e*	0.0138(12)	0.0176(13)	0.0151(13)	0.00000
Mg3	4*i*	0.0162(10)	0.0248(11)	0.0149(9)	0.0004(8)
Mg4	4*i*	0.0167(10)	0.0244(11)	0.0171(10)	0.0000(8)
Mg5	2*f*	0.0156(13)	0.0249(15)	0.0229(15)	0.00000

broken symmetry solution; because the *R* atoms sit in three independent sites (4*j*, 2*f*, and 2*f*), the starting density for the 4*f* site was assigned spin-up and those for the other two sites as spin-down. Moreover, all atomic positions were further optimized by keeping the unit cell parameters constant for all three compounds.

DFT/PBE[35] quantum chemical calculations were performed for $LuCuMg_2$ by means of the all-electron full-potential local orbital (FPLO) code.[36] The compound with *R* = Lu was selected to avoid partially filled 4*f* states. The experimentally determined lattice spacings were used, and the atomic positions optimized using as input those refined based on the single-crystal X-ray diffraction data for $DyCuMg_2$. Relativistic effects were treated at the scalar relativistic level, and the Brillouin zone sampling was conducted with a (4 14 4) *k*-point mesh. To investigate the chemical bonding by position-space techniques,[37] the electron density (ED) and the electron localizability indicator, in its ELI-D[38,39] representation, were calculated using an equidistant grid of about 0.05 Bohr by means of a dedicated module implemented within the FPLO code.[40] The topological analysis of both fields was performed based on the quantum theory of atoms in molecules (QTAIM)[41] with the DGrid[42] software. The QTAIM/ELI-D intersection technique[43] was employed to evaluate the contribution, in terms of the electronic population, of a QTAIM atom (X) intersecting an ELI-D basin (B_i), quantified with the bond fraction $p(B_i^X)$.[44,45] The ED, the ELI-D and their basins were displayed with the ParaView visualization application thanks to specifically designed plug-ins.[46]

3. Results and discussion

3.1. Crystal structure

The samples of interest turned out to be almost $RCuMg_2$ single-phase (see Table 3), with small quantities of a secondary compound, with an average composition of ~16.7 at% *R*, 16.7 at% Cu, and 66.6 at% Mg, compatible with the $RCuMg_4$ stoichiometry.

Table 3 Results of the SEM-EDXS and PXRD characterizations of samples with a $R_{25}Cu_{25}Mg_{50}$ nominal composition

		Crystal structure: *oP*32-$DyCuMg_2$ Lattice parameters (Å)		
Overall composition (at%)	$RCuMg_2$ composition *R*; Cu; Mg (at%)	*a*	*b*	*c*
1-$Dy_{24.4}Cu_{23.3}Mg_{52.3}$	23.8; 23.4; 52.8	13.530(5)	3.755(1)	13.793(4)
2-$Ho_{26.8}Cu_{24.0}Mg_{49.2}$	24.6; 23.6; 51.8	13.506(4)	3.737(1)	13.785(4)
3-$Er_{24.3}Cu_{24.4}Mg_{51.3}$	24.2; 25.0; 50.8	13.462(3)	3.720(1)	13.781(4)
4-$Tm_{25.6}Cu_{24.3}Mg_{50.1}$	26.2; 23.8; 50.0	13.452(3)	3.700(1)	13.779(3)
5-$Lu_{24.4}Cu_{25.4}Mg_{50.2}$	23.5; 24.2; 52.3	13.409(4)	3.6655(9)	13.773(3)

Powder X-ray diffraction analysis confirmed that the samples are almost single-phase and that all five compounds are isostructural, belonging to the orthorhombic $DyCuMg_2$ prototype (see Fig. 2).

As expected, a regular peak shift towards higher angles is observed when increasing the atomic number of the R component (see Fig. 2, inset), corresponding to a decrease in the lattice parameters due to the lanthanide contraction. The cell volume is plotted in Fig. 3 as a function of the R^{3+} ionic radius,[47] showing a perfectly linear trend. The percentage volume contraction is a qualitative indicator of all types of interactions in solids, especially useful when comparing related series of compounds.[48,49] This parameter was calculated for the title compounds, according to the formula $\Delta V(\%) = 100 \times \frac{V_{meas} - V_{calc}}{V_{calc}}$, where $V_{calc} = \Sigma_i N_i \times V_i$ (N_i = number of i-type atoms in the unit cell, V_i = atomic volume of the i-type species taken from ref. 50) and V_{meas} is the experimentally determined volume. Negative $\Delta V(\%)$ values (in the range from −2.5 to −3.7%) are obtained for all compounds, decreasing regularly as a function of the R component dimensions (see Fig. 3) and indicating interactions between components somewhat stronger with respect to pure metals.

For comparison, $\Delta V(\%)$ was also calculated for the complete R_2Cu_2Mg series (R = La, Ce–Nd, Sm, Gd–Lu), considering its structural relationships with $RCuMg_2$ (see below). For the Dy–Lu subset, similar values and a decreasing trend are obtained (from −2.5 to −4.7%), as can be seen in Fig. S1.

Considering the Dy representative, the minimum interatomic distances in the 1:1:2 structure are Cu–Mg (2.678 Å) and Cu–Dy (2.896 Å), somewhat shorter than the metallic radii sums.[51] Instead, the numerous Mg–Mg contacts range between 3.092 and 3.759 Å, which are common distances for intermetallics. The shortest interatomic distances for all the species are listed in Table 4. The coordination polyhedra of the smallest Cu atoms are three-capped trigonal prisms, with two different compositions Cu@Dy6CuMg2 and Cu@Dy4Mg5. The coordination topology of the different Mg species can be envisaged as derived from a rhombic dodecahedron (CN = 8 + 6), more or less distorted. Visualising a larger portion of the structure, what catches the eye is the presence of clusters formed by four trigonal prisms sharing edges to create a cubic-like cavity occupied by a Mg atom. This star-like structural fragment is typical of the ubiquitous Mo_2FeB_2 structure type, also

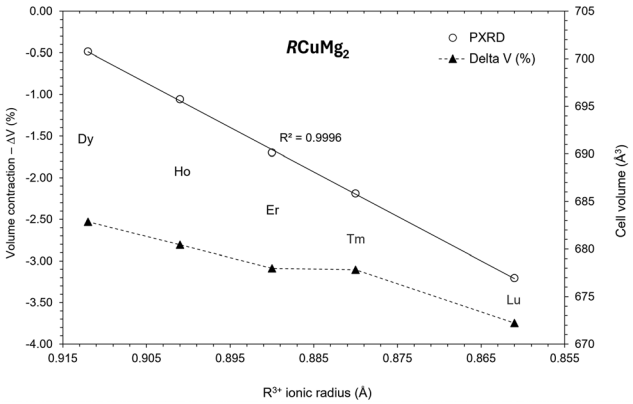

Fig. 3 Unit cell volume and volume contraction trends for $RCuMg_2$ compounds.

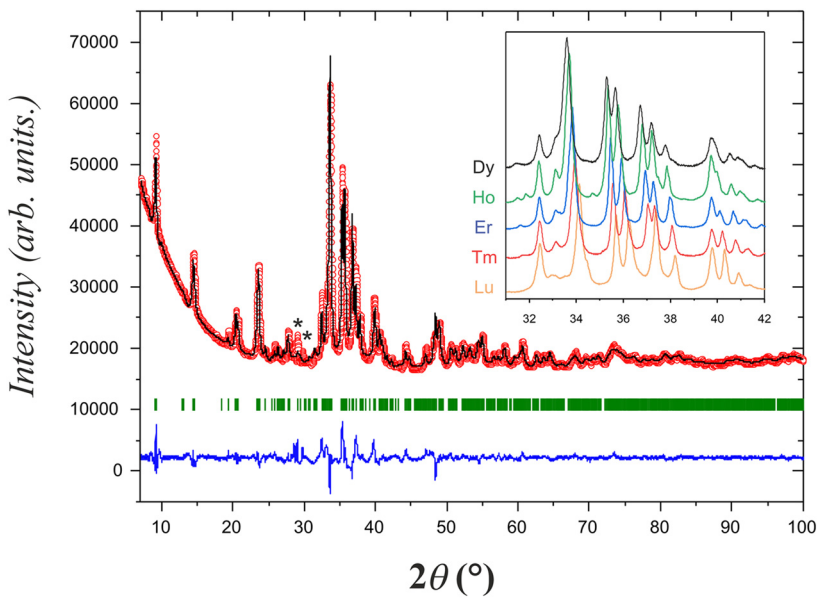

Fig. 2 Observed (red circles), calculated (black line) and difference (bottom blue line) X-ray powder diffraction patterns of the $Dy_{25.0}Cu_{25.0}Mg_{50.0}$ sample. Vertical bars indicate the Bragg positions of the $DyCuMg_2$ phase (R_B = 0.0951; R_F = 0.0494; R_p = 0.198; R_{wp} = 0.198); the most intense peaks of the secondary phase are indicated with *. The relative shift of experimental diffraction peaks for other $RCuMg_2$ compounds is shown in the 2θ range from 31 to 42° (inset).

Table 4 Interatomic distances (<4 Å) for $DyCuMg_2$, as obtained from single crystal data

Central atom	Adjacent atoms	Distance (Å)	Central atom	Adjacent atoms	Distance (Å)
Dy1	2× Cu2	2.9316(6)	Mg1	2× Cu2	2.6785(16)
	2× Cu1	2.9357(6)		2× Mg4	3.0923(24)
	2× Cu1	2.9472(6)		2× Mg3	3.1056(24)
	2× Mg2	3.3206(2)		2× Mg4	3.1451(24)
	2× Mg3	3.3849(18)		1× Mg5	3.2542(22)
	1× Mg1	3.5836(21)		1× Mg1	3.3926(29)
	1× Dy1	3.6581(4)		1× Dy1	3.5836(21)
	2× Dy1	3.7594(1)		1× Dy2	3.6144(22)
	1× Dy2	3.8208(4)		2× Mg1	3.7594(1)
	1× Dy3	3.8972(4)	Mg2	2× Cu1	3.0206(21)
Dy2	4× Cu2	2.8956(6)		2× Cu2	3.0797(21)
	2× Mg2	3.2931(23)		2× Dy2	3.2931(23)
	4× Mg4	3.3839(18)		2× Dy3	3.3197(23)
	2× Mg1	3.6144(22)		4× Dy1	3.3206(2)
	2× Dy2	3.7594(1)		2× Mg2	3.7594(1)
	2× Dy1	3.8208(4)	Mg3	1× Cu1	2.8554(22)
Dy3	4× Cu1	2.9083(5)		1× Cu2	2.9846(23)
	2× Mg2	3.3197(23)		2× Mg1	3.1056(24)
	4× Mg3	3.3695(18)		2× Mg5	3.1193(23)
	2× Dy3	3.7594(1)		2× Dy3	3.3695(18)
	2× Dy1	3.8972(4)		2× Dy1	3.3849(18)
Cu1	1× Cu1	2.6635(10)		1× Mg3	3.3985(31)
	1× Mg3	2.8554(22)		2× Mg3	3.7594(1)
	2× Dy3	2.9083(5)		1× Mg4	3.8069(29)
	2× Dy1	2.9357(6)	Mg4	1× Cu2	2.8851(22)
	2× Dy1	2.9472(6)		2× Mg1	3.0923(24)
	1× Mg2	3.0206(21)		2× Mg1	3.1451(24)
	2× Cu1	3.7594(1)		1× Mg4	3.1477(33)
Cu2	2× Mg1	2.6785(16)		2× Mg5	3.1548(25)
	1× Mg4	2.8851(22)		2× Dy2	3.3839(18)
	2× Dy2	2.8956(6)		1× Mg4	3.6421(33)
	2× Dy1	2.9316(6)		2× Mg4	3.7594(1)
	1× Mg3	2.9846(23)		1× Mg3	3.8069(29)
	1× Mg2	3.0797(21)	Mg5	4× Mg3	3.1193(23)
	2× Cu2	3.7594(1)		4× Mg4	3.1548(25)
				2× Mg1	3.2542(22)
				2× Mg5	3.7594(1)

adopted by R_2Cu_2Mg compounds. This similarity was the starting point of a comparative structural analysis of some compounds existing in these systems (see Fig. 1 and 4).

Because their *R*/Cu ratios are constant, it is convenient to examine these compounds in the ascending order of the Mg content. In the case of R_2Cu_2Mg, the crystal space is filled by the star-like clusters, with no gaps in between; therefore, Mg atoms are only located at the centre of the clusters.

With increasing Mg concentration, in the $RCuMg_2$ compounds, 2D wavy arrangements of these building blocks are alternated with Mg strips with a three-atomic-layer thickness. It is interesting to note that the Mg matrix possesses a *bcc*-like topology, instead of the *hcp* adopted by the pure element. This topology perfectly matches the clusters' shape. The observed trend is even more evident when considering the Mg-richer $RCuMg_4$ compounds. In their structure, the same clusters are further diluted, adopting a 1D distribution in a Mg matrix, which still has a *bcc*-like topology. Following the proposed description, the dilution of star-like clusters with magnesium can be schematized as follows:

$$R_2Cu_2Mg \xrightarrow{+3Mg} 2RCuMg_2 \xrightarrow{+4Mg} 2RCuMg_4$$

Considering the nature of constituents, the structural peculiarities, and the localization of the *R* component in common building blocks, both a chemical bonding analysis and a comparison of the magnetic properties of these compounds are discussed below.

3.2. Chemical bonding

The calculated electronic density of states (DOS, Fig. 5) for the $LuCuMg_2$ compound, chosen as a representative, reveals it to be a metallic conductor, as indicated by the non-zero number of states at the Fermi level.

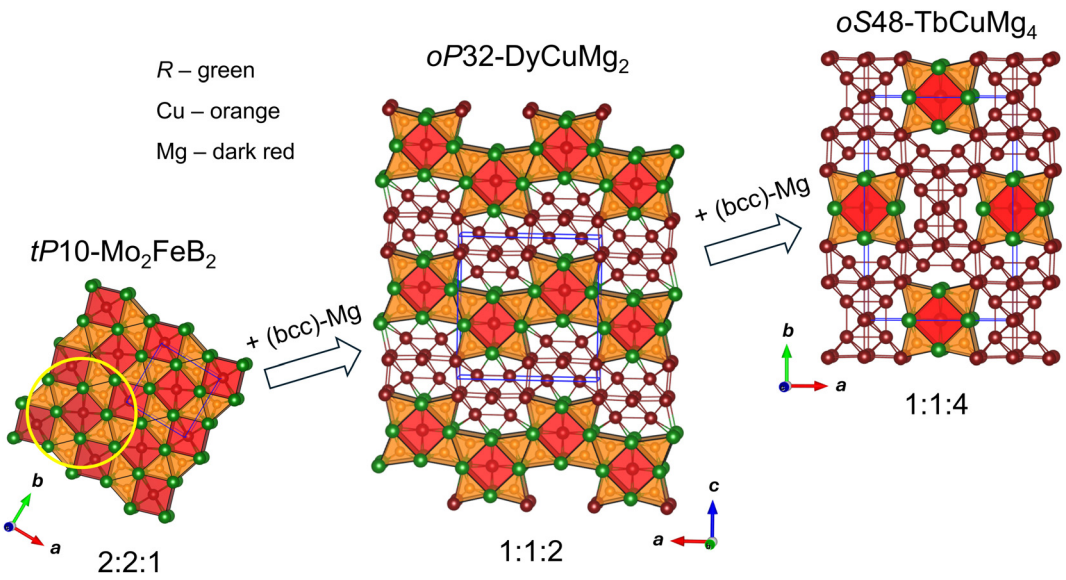

Fig. 4 Crystal structure relationships between R_2Cu_2Mg, $RCuMg_2$ and $RCuMg_4$ compounds. Structures are projected along the shortest lattice vector, and unit cells are shown in blue. As a guide for the eye, one star-like cluster is highlighted by a yellow circle.

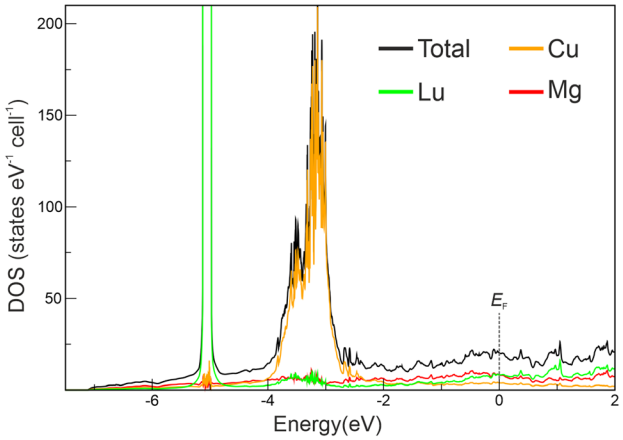

Fig. 5 Total and species-projected electronic density of states (DOS/pDOS) for $LuCuMg_2$.

The narrow peak around −5 eV corresponds to the filled and localized Lu 4*f* states, whereas the broader region between approximately −2.5 and −4 eV is mainly contributed to by the filled Cu 3*d* states. Near the Fermi level (E_F), the DOS is mainly dominated by Mg 3*p* and Lu 5*d* states.

To get further insights into the chemical interactions among the constituents, position-space quantum-chemical techniques were selected. The calculated effective charges indicate that Lu and Cu act as the QTAIM cation and anion, respectively, regardless of the occupied Wyckoff position (see Fig. 6).

Therefore, $LuCuMg_2$ enriches the family of intermetallics with anionic transition metals, which have recently been increasingly studied owing to their often intriguing structural, physical and chemical properties.[52–59] Focusing on the two copper species, the difference between the charges of Cu1 and Cu2 (−1.74 *vs.* −2.34) can initially be attributed to the fact that Cu1 has another Cu1 neighbor ($d_{Cu1-Cu1}$ = 2.64 Å), as indicated by a large flat basin surface, quite typically observed for homo-contacts (orange basin in Fig. 6).[33,60–63] The situation of the Mg atoms is more heterogeneous. In fact, all species are cationic except for Mg5, which shows a small negative charge (yellow basin in Fig. 6). Mg2, the only one not belonging to the *bcc*-like slab, bears the largest positive charge of +0.90, followed by Mg3, Mg1, and Mg4, all having, in addition to other Mg atoms, both Cu and Lu in their coordination sphere. The trend observed in the magnesium charges can be rationalized by considering the number of more electronegative atoms in its coordination environment, namely, Cu. At this stage of the discussion, the approximation of neglecting Lu is justified by the longer Mg–Lu distances compared to the Mg–Cu ones. Mg2 (+0.90) is coordinated by four Cu atoms, while both Mg3 and Mg1 are coordinated by two Cu atoms and exhibit similar charges (+0.65 and +0.56, respectively). Mg4 (+0.33), in contrast, is coordinated by only one Cu atom. Mg5 has a noticeably different coordination environment, comprising only Mg species. It is located at the centre of the *bcc* unit, which may cause its low negative charge, the origin of which will be further elucidated through the QTAIM/ELI-D intersection.

The average effective charges of +1.10 for Lu, +0.47 for Mg and −2.04 for Cu suggest classifying $LuMg_2Cu$ as an intermetallic cupride, analogous to the $LaMg_2Au$ auride.[14] Interestingly, a bonding analysis based on orbital-based techniques was recently conducted for $YCuMg_4$ [64] (*o*S48-$TbCuMg_4$), which is structurally related to the title compound, as displayed in Fig. 4. In that case, the calculated Löwdin charges indicate that both yttrium and copper act as cations, while the magnesium species get either zero or increasingly negative

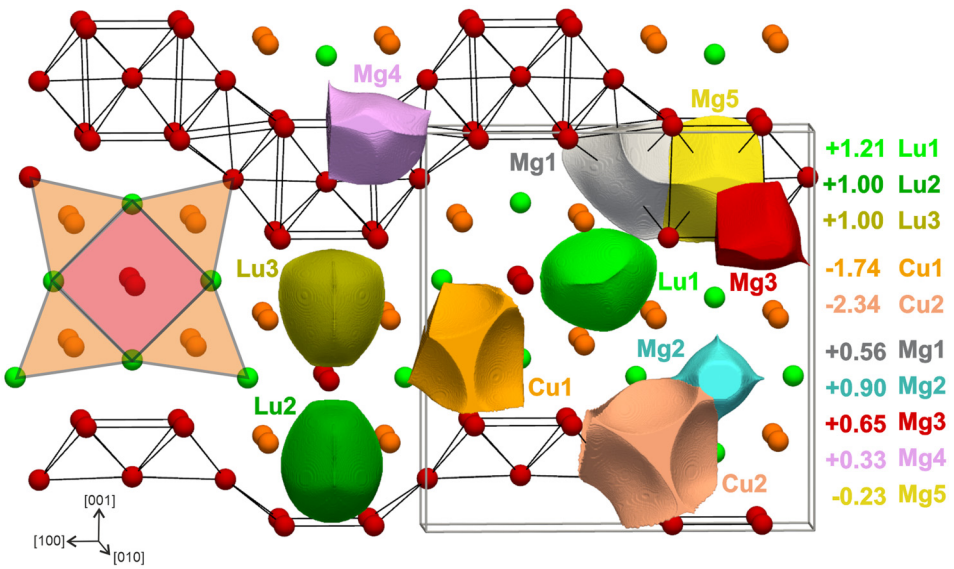

Fig. 6 Shapes and effective charges of QTAIM atomic basins for $LuCuMg_2$. Black sticks indicate Mg–Mg contacts within the *bcc*-like slabs, while the red square and orange triangles highlight the star-like clusters.

values as the number of Cu neighbours increases. It is important to highlight that because QTAIM and Löwdin charges are defined on completely different bases, their numerical values may differ significantly and should not be directly compared. Nevertheless, it is highly interesting to observe which overall description of related compounds emerges when different methods are applied. Reimann *et al.*[64] claimed that the covalent character of the Mg–Mg bonds in $YCuMg_4$ is responsible for this trend, although the charge values seem to contradict the electronegativity difference between Cu and Mg. In our case, the charge transfer better follows the electronegativity differences. A reasonable explanation for the low effective charge of Mg with respect to its formal value observed in $LuCuMg_2$ is the involvement of magnesium in covalent interactions, hinting toward a consistent picture.

Further insights were obtained through a topological analysis of the ELI-D along with the intersection of its basins with the QTAIM ones.

Several ELI-D attractors (maxima) are found in the crystal space around Mg species in the *bcc*-like slab and in the inner zone of the star-like cluster between Mg2, Lu and Cu species, as indicated by its planar distribution (Fig. 7a) and isosurfaces (Fig. 7b and c).

More specifically, ELI-D attractors in the *bcc* slab located in tetrahedral interstices are pointed out in Fig. 7b by three types of irreducible and one type of reducible localization domain. The latter, located between the Mg4–Mg4 contact, encloses two types of maxima (Fig. 7a in the (010) plane): one in the interstitial tetrahedral $Mg4_2Mg5_2$ site and the other in the region between Mg4 and neighbouring Cu2 and Lu2. Isosurfaces at lower ELI-D values (Fig. 7c) enable the visualization of attractors within the star-like clusters, while a single reducible domain encloses all maxima within the *bcc* slab as well as those between the slab and the surrounding Cu and Lu atoms. Focusing on the region of the star-like cluster, an attractor is situated between Mg2 atoms, in a sort of octahedral interstice, surrounded by four Lu and two Mg2 species and further by eight Cu atoms (similar to the octahedral interstices in a *fcc* lattice, Fig. 7a and c). In this region, numerous maxima of the ELI-D are also located, and the positions of some are indicated by the isosurfaces shown in Fig. 7c. These findings reveal a rather complex overall topology characterized by approximately twenty distinct types of ELI-D attractors in the valence region. In this case, it is convenient to visualize the bonding situation using basin sets. ELI-D basins with attractors higher than 1.06 and having a common isosurface were merged. In this way, only two types of basin sets were obtained: one that surrounds and incorporates the *bcc* Mg layer (blue in Fig. 8a) and the other shared along [010] between the *fcc*-like clusters (green in Fig. 8a).

Within these basin sets, two groups of ELI-D multiatomic (atomicity $a \geq 3$) bonds can be distinguished: homoatomic, contributed almost exclusively by Mg atoms, and heteroatomic. The blue basin set in Fig. 8a is formed by both homo- and het-

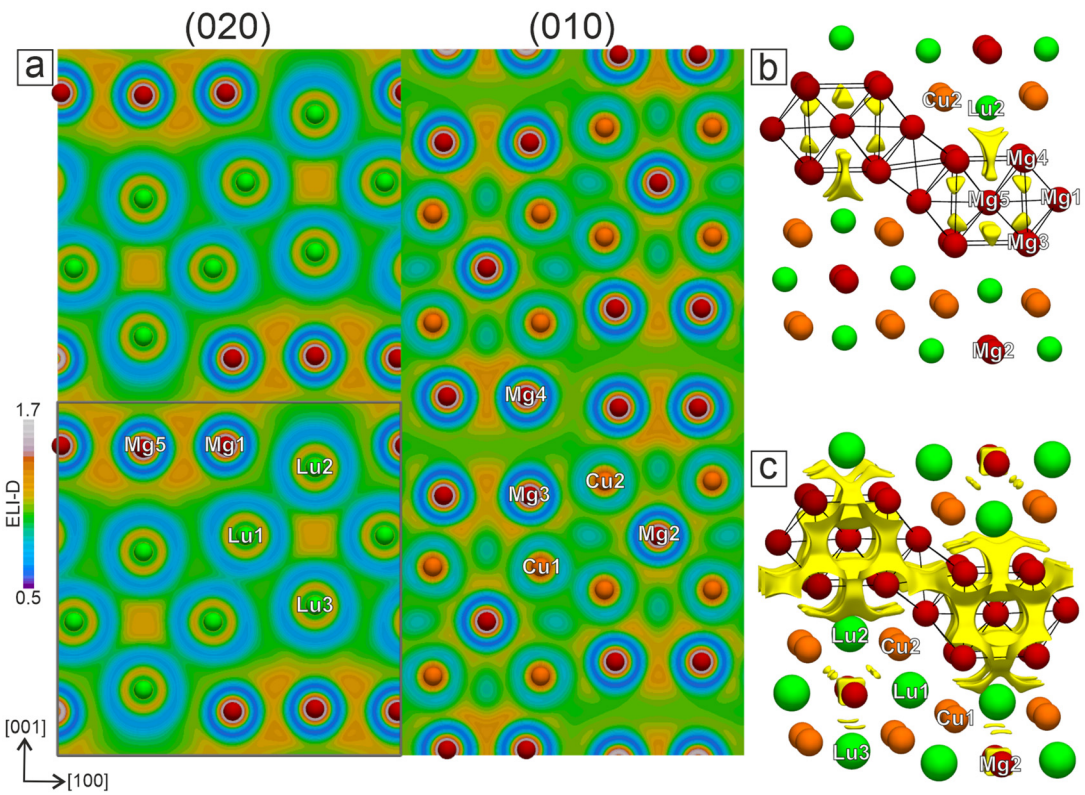

Fig. 7 ELI-D planar distribution (a) in the (020) and (010) planes together with 1.21 (b) and 1.14 (c) localization domains of ELI-D.

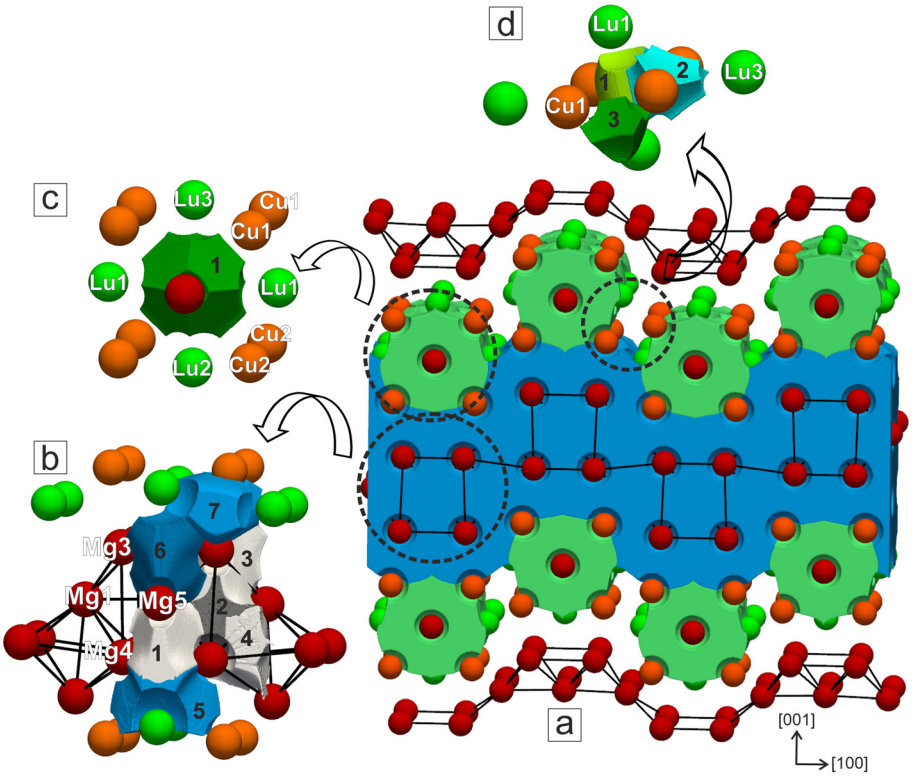

Fig. 8 ELI-D basin sets (a) and bond basins (b, c, d) for $LuCuMg_2$.

eroatomic basins, whereas the green one is formed only by heteroatomic basins. Fig. 8b shows the most populated ELI-D basins located within and around the *bcc* slab. Specifically, homoatomic (Fig. 8b, basins 1–4) and heteroatomic (Fig. 8b, basins 5–7) bonds are displayed in grey and blue, respectively. The four homoatomic ones involve three or four Mg, with the bond population in all cases almost entirely contributed by Mg QTAIM atoms (see Table 5). This is evidenced by the total bond fraction of Mg $p(B_i^{Mg}) \geq 0.94$, resulting in effectively 3- and 4-atomic bonds (3*a* or 4*a*; see Table 5).

A similar scenario, with many Mg homoatomic interactions, was recently observed in the complex $Mg_{29-x}Pt_{4+y}$ intermetallic;[52] interestingly, this is not the case for the $LaAuMg_2$ compound.[14]

Heteroatomic basins 5 and 7 in Fig. 8b are both contributed by all elements, resulting in 6*a* bonds, while basin 6 is 4*a* with no contribution from Cu.

At this point, the origin of the slight negative charge on Mg5 may be traced by intersecting the Mg5 QTAIM atom with the adjacent ELI-D basins. The contribution from the Mg5 core basin is 10.09 e^-, and 1.70 e^- and 0.44 e^- are contributed by seven homoatomic and two heteroatomic bonds, respectively, yielding, for this species, a total average population of 12.23 e^-.

The largest and most populated heteroatomic basin in the green basin set is labeled with number 1 in Fig. 8c; this is the bond showing the largest atomicity of 14 (see Table 5), located

Table 5 Average electronic populations $\bar{N}(B_i)$ and bond fractions for the ELI-D basins B_i of $LuCuMg_2$ displayed in Fig. 8. The numbers used to label basins are the same as those shown in Fig. 8b–d

	ELI-D basin (B_i)	Atomicity $Mg_nCu_kLu_h$	$\bar{N}(B_i)$	$\sum_{j=1}^{n} p\left(B_i^{Mg_j}\right)$	$\sum_{j=1}^{k} p\left(B_i^{Cu_j}\right)$	$\sum_{j=1}^{h} p\left(B_i^{Lu_j}\right)$
Fig. 8b	1	Mg_4Lu_2	0.83	0.99	—	0.01
	2	Mg_3Cu_1	0.64	0.99	0.01	—
	3	$Mg_4Cu_2Lu_2$	1.06	0.94	0.03	0.03
	4	Mg_3Cu_2	0.39	0.94	0.06	—
	5	$Mg_2Cu_2Lu_2$	2.09	0.37	0.40	0.23
	6	Mg_3Lu_1	0.75	0.88	—	0.12
	7	$Mg_1Cu_1Lu_4$	1.90	0.12	0.66	0.22
Fig. 8c	1	$Mg_2Cu_8Lu_4$	1.13	0.47	0.13	0.40
Fig. 8d	1	Cu_2Lu_2	0.62	—	0.80	0.20
	2	Cu_2Lu_3	0.43	—	0.77	0.23
	3	Cu_2Lu_2	0.50	—	0.83	0.17

in the above-mentioned octahedral-like Mg_2Lu_4 interstitial site. It has to be noted that the eight Cu atoms located on the vertices of the *fcc* cluster contribute just 0.15 electrons, corresponding to a total bond fraction of 0.13 (see Table 5).

Three types of ELI-D attractors not included in the blue and green basin sets (because their values are lower than 1.06) are located in the columns formed by condensed $Cu1_4Lu1_2$ distorted octahedra. Their basins (1, 2 and 3 in Fig. 8d) are the only ones exclusively contributed by Lu and Cu (see Table 5). These are 4*a* (basins 1 and 3) and 5*a* (basin 2) polar bonds, where the main contribution to the population is made by the most electronegative copper atoms; the total bond fraction for copper is $0.77 \leq p(B_i^{Cu}) \leq 0.83$. Therefore, no 2*a* polar *R*–*T* bonds indicated by bulges of the copper penultimate shell have been found, contrary to the case of Au–La in $LaAuMg_2$.[14] This difference between the transition metals of the fourth period and those below is similar to that observed for other ternary rare earth intermetallics.[62]

In summary, the chemical bonding scenario in $LuCuMg_2$ is highly heterogeneous, involving both homoatomic and heteroatomic interactions. The overall picture is further complicated by the presence of distinct types of heteroatomic bonds, some involving all three elements, while others occurring exclusively between Lu cations and Cu anions. As suggested by the partitioning of space obtained through basin sets, three distinct regions can be identified. The first one corresponds to the *bcc*-like Mg slabs and the region between them and the adjacent Cu and Lu atoms. In this area, the bonding scenario is characterized by homoatomic 3*a* and 4*a* bonds realized within the Mg slabs, which interact with surrounding Lu and Cu atoms *via* heteroatomic 4*a* and 6*a* interactions. The second region is located at the centre of star-like clusters. This area consists of *fcc*-like units (8 Cu, 4 Lu, and 2 Mg) condensed along the [010] direction, where multiatomic heteroatomic interactions are realized. The third region comprises the remaining crystal space. Here, heteroatomic interactions are still observed, with atomicities of 4 or 5, but notably, Mg is not involved, marking a clear distinction from the previous regions. Therefore, it can be concluded that $LuCuMg_2$ exhibits bonding inhomogeneity, a feature also recently observed in $Mg_{29-x}Pt_{4+y}$, despite structural differences between the two compounds. These findings provide further evidence of the chemical tendency of Mg to segregate within the crystal space of certain intermetallic phases, resulting in homoatomic bonds. A similar bonding inhomogeneity may be supposed for the LPSO phases as well, with similar structural features.[21]

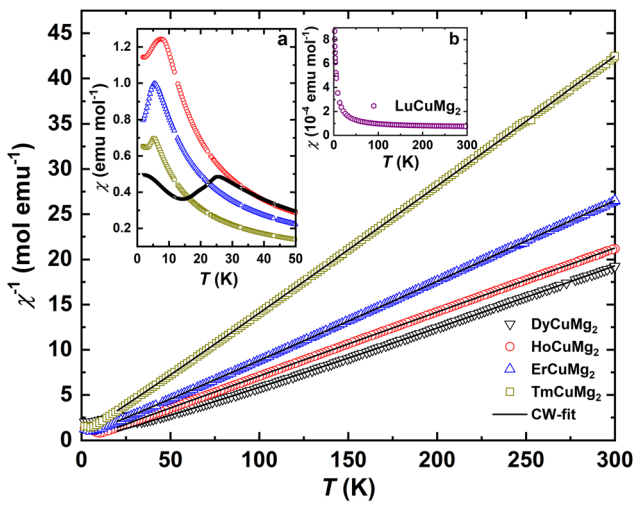

Fig. 9 Temperature dependencies of the reciprocal magnetic susceptibility $\chi^{-1}(T)$ at $\mu_0 H$ = 1 T for RCuMg$_2$ compounds together with Curie–Weiss fits. Inset (a) magnetic susceptibility $\chi(T)$ of RCuMg$_2$ at the antiferromagnetic transitions; (b) magnetic susceptibility $\chi(T)$ of $LuCuMg_2$.

3.3. Physical properties

The temperature dependencies of the reciprocal magnetic susceptibility $\chi^{-1}(T)$ of selected RCuMg$_2$ compounds are depicted in Fig. 9. They are linear in a broad *T*-range (20–300 K) and thus fit well to the modified Curie–Weiss (CW) law: $\chi = C/(T - \theta_{CW})$. The deviation from the linearity of $\chi^{-1}(T)$ for $DyCuMg_2$ at much higher (in comparison with other isostructural compounds) $T \approx 80$ K can be explained by (i) the enhanced ordering temperature (T_N) and/or (ii) the stronger crystal electric field (CEF) effects. The parameters deduced from CW fits are presented in Table 6. The obtained effective magnetic moments $\mu_{eff}^{exp} = \sqrt{3k_B C/N_A}$ are in good agreement with the theoretically deduced values for R^{3+} ions. The negative θ_{CW} values hint towards antiferromagnetic interactions in the studied materials. Instead, the positive θ_{CW} for $DyCuMg_2$ is due to the narrow *T*-range used in the fit.

In agreement with the negative Curie–Weiss temperatures, all studied RCuMg$_2$ order most probably antiferromagnetically, with their critical temperatures T_N listed in Table 6. This is reflected in the broad cusps clearly visible in the temperature dependencies of magnetic susceptibility $\chi(T)$ (Fig. 9, inset a). The magnetic structure of $DyCuMg_2$ seems to be of a more complex character, because the well pronounced shoulder at $T_{N_2}^{\chi} = 20.5(9)$ K becomes clearly visible. Notably, the anomalies in the antiferromagnetic orderings of the isostructural RCuMg$_2$ are remarkably broadened in $\chi(T)$ dependencies; the

Table 6 Magnetic characteristics of RCuMg$_2$

Compound	*T*-range (K)	μ_{eff}^{theor} (μ_B)	μ_{eff}^{exp} (μ_B)	θ_{CW} (K)	$T_{N_1}^{\chi}$ (K)	$T_{N_2}^{\chi}$ (K)	$T_{N_1}^{c_p}$ (K)	$T_{N_2}^{c_p}$ (K)	$T_{N_3}^{c_p}$ (K)
$DyCuMg_2$	80–300	10.65	10.77(9)	3.0(1)	25.5(9)	20.5(9)			
$HoCuMg_2$	20–300	10.61	10.71(9)	−0.6(1)	7.5(9)				
$ErCuMg_2$	20–300	9.58	9.67(9)	−3.3(1)	5.5(9)		8.6(3)	6.6(3)	5.7(3)
$TmCuMg_2$	20–300	7.56	7.71(9)	−4.1(1)	5.3(9)		6.1(3)	4.8(3)	3.3(3)

measurements of the specific heat capacity indicate multiple transitions for them (see discussion below).

The magnetic susceptibility of $LuCuMg_2$ (Fig. 9, inset b) is positive, it is about 3 orders of magnitude lower than those of other $RCuMg_2$ and is weakly temperature-dependent at 100 K < T < 300 K [χ_0 = 6.6(1) × 10^{-5} emu mol^{-1}, which corresponds to the density of states at the Fermi level $N(E_F)$ = 2.1 state eV^{-1} f.u.$^{-1}$, in fair agreement with the specific heat data]. All these features indicate that $LuCuMg_2$ is a Pauli paramagnet. The strong upturn in $\chi(T)$ below ≈50 K is due to a minor paramagnetic impurity (<0.1 vol%), which is not detectable by XRD and EDX.

The temperature dependencies of the specific heat capacity $c_p(T)$ of $RCuMg_2$ (R = Er, Tm, Lu) under different magnetic fields are depicted in Fig. 10. The anomalies due to the antiferromagnetic ordering for compounds containing magnetic rare-earth elements reveal additional bumps and shoulders, thus indicating multiple transitions. The $T_{N_i}^{c_p}$ values at which they occur are presented in Table 6. Interestingly, the best coincidence of $T_{N_i}^{\chi}$ is observed with $T_{N_3}^{c_p}$ for Er and $T_{N_2}^{c_p}$ for Tm. Because all observed anomalies will be suppressed with increasing magnetic field, one can suggest that they have an antiferromagnetic origin. To shed light on the possible magnetic ordering, the total energies of the optimized structural models (standardized relaxed atomic coordinates are presented in Table S1) in ferromagnetic and antiferromagnetic cases were calculated (Table 7). The obtained electronic densities of states (DOS) and band structures are depicted in Fig. S2–S4. As can be seen from the projected DOS, the bands close to the Fermi level are dominated by the corresponding f-electrons of the rare-earth metal.

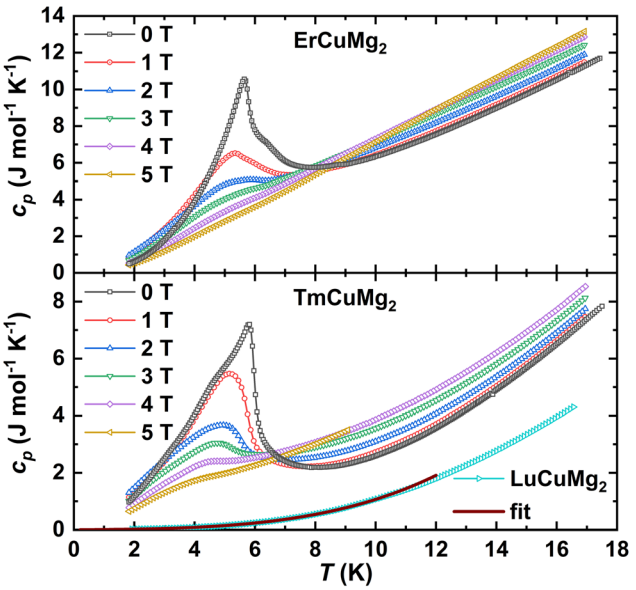

Fig. 10 Temperature dependencies of the specific heat capacities of $RCuMg_2$ (R = Er, Tm, Lu) under different magnetic fields. For $LuCuMg_2$, the fit for the $c_p(T) = \gamma T + \beta T^3 + \delta T^5$ ansatz is shown.

Table 7 Total energies (in Ry) of the optimized structural models for antiferromagnetic (AFM) and ferromagnetic (FM) cases

	$DyCuMg_2$	$HoCuMg_2$	$ErCuMg_2$
AFM	−227 486.29782	−234 847.44499	−242 385.31189
FM	−227 486.22978	−234 847.57351	−242 385.03028

In the cases of $DyCuMg_2$ and $ErCuMg_2$, the antiferromagnetic solution has a lower energy, whereas for $HoCuMg_2$, the ferromagnetic solution appears to be more favourable. At first glance, the latter result looks like a discrepancy with experimental data. However, considering the complexity of the magnetic interactions in the title compounds, which are characterized by multiple transitions [the broadened ordering at T_N = 7.5(9) for $HoCuMg_2$ could be obviously resolved in a $c_p(T)$ dependence], one would need to account for other variants (*e.g.*, canting of the spins and different ferromagnetic arrangements) to speculate about the reliable spin configurations in the studied series. Moreover, it is worth mentioning that starting from the optimized atomic positions of the AFM case and performing a single-point FM calculation (without further geometrical optimization), a total energy slightly below the AFM solution is obtained (Table 7). This suggests that small changes in the atomic positions may affect the results of magnetic behaviour simulations. Obviously, to finally and unambiguously shed light on the nature of the transitions, the complex magnetic structures of $RCuMg_2$ should be investigated *via* neutron diffraction.

In the temperature range of 1.8–7 K, the specific heat of the non-magnetic phonon reference compound $LuCuMg_2$ fits well to the $c_p(T) = \gamma T + \beta T^3 + \delta T^5$ *ansatz*, with the Sommerfeld coefficient of the electronic contribution (c_{el}) γ = 6.58(8) mJ mol^{-1} K^{-2} [corresponds to $N(E_F)$ = 2.8 state eV^{-1} f.u.$^{-1}$], phononic terms (characteristic of c_{ph}) β = 0.86(7) mJ mol^{-1} K^{-4} (indicates Debye temperature θ_D = 209 K) and δ = 1.6(7) × 10^{-3} mJ mol^{-1} K^{-4}.

Further, we subtracted the specific heat of the phonon reference $LuCuMg_2$ from that of $RCuMg_2$ (R = Er, Tm) and obtained magnetic contributions (c_{mag}) to their $c_p(T)$ (Fig. 11). By calculating c_{mag}/T and integrating it, we found the temperature evolution of magnetic entropy in the studied compounds (Fig. 11, inset). In both cases, their values are smaller than Rln2 at the antiferromagnetic transitions and thus well below the theoretically expected Rln4 and Rln3 for Er^{3+} and Tm^{3+} ions, respectively. Such a strong discrepancy between these values may indicate that the classical LS coupling scheme is not adequate for $RCuMg_2$, and one of the possible reasons for this could be the enhanced level of itineracy of 4f electrons in the compounds.

The specific heat of $LuCuMg_2$ in the $c_p/T^3(T)$-presentation (Fig. 12) reveals a well-pronounced maximum centred at T_f ≈ 12 K. This is a signature of the strong contribution of the Einstein optical modes to the specific heat.[65,66] One of the possible reasons for such behaviour is the so-called 'rattling' effect arising from the scattering of the phonons on weakly bound and thus strongly vibrating atoms. The enhanced value

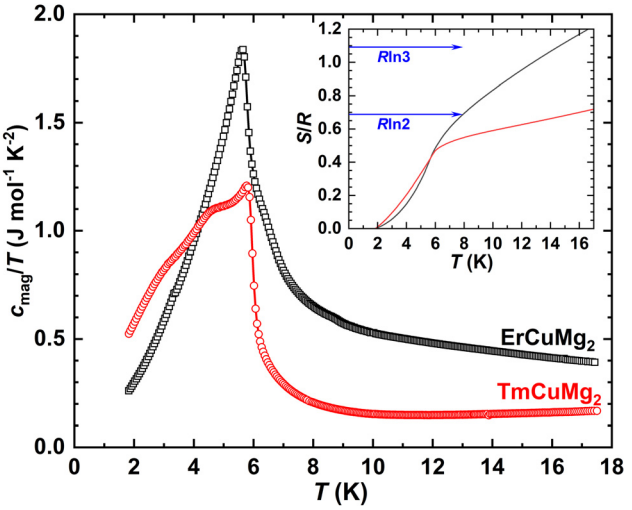

Fig. 11 Temperature dependencies of the magnetic specific heat of RCuMg$_2$ (R = Er, Tm) obtained after the subtraction of phonon reference LuCuMg$_2$. Inset: Temperature evolution of the entropy near magnetic transitions.

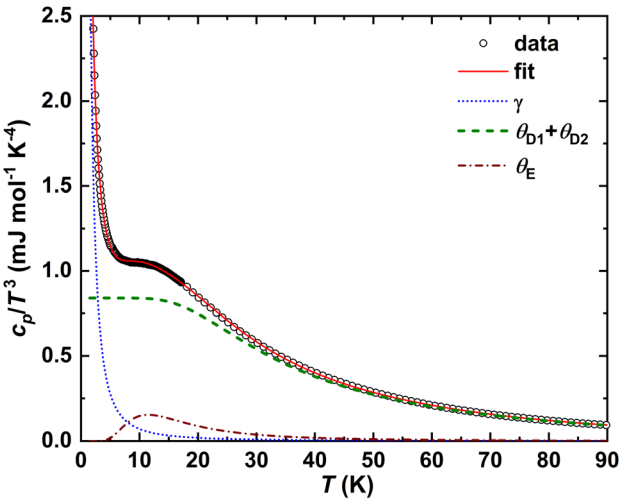

Fig. 12 Temperature dependence of the specific heat of LuCuMg$_2$ in the $c_p/T^3(T)$ presentation together with the fit to eqn (1) (red line) as well as separate Debye (eqn (2)), Einstein (eqn (3)) and electronic contributions.

of the thermal displacement parameter for the Mg5-atom in the 2*f* site (Table 2), which is obviously because this atom centres an enlarged [Dy8Cu4] cuboctahedron (Fig. 4), suggests that it is a possible candidate for this phenomenon. However, to confirm this assumption, the temperature evolution of its thermal displacement parameter should be studied.

Despite the lack of solid evidence for 'rattling' in LuCuMg$_2$, we tried to describe its $c_p/T^3(T)$ using the model given in eqn (1). For this purpose, the heavier Lu and Cu atoms were assumed to form a framework providing six Debye modes (N_{D1} = 6), whereas the lighter magnesium atoms were expected to be responsible for other ones (N_{D2}). Thus, having 16 Mg atoms in the unit cell, from which 2 were 'rattlers', N_{D2} and N_E were expected to be 5.25 and 0.75, respectively. Hence, the total number of modes should be $N_{tot} = N_{D1} + N_{D2} + N_E = 12$. Further, the fit to eqn (1) with two Debye (eqn (2)) and one Einstein (eqn (3)) contributions resulted in N_{D1} = 9.6(5), N_{D2} = 3.2(2), and N_E = 0.2(1), with the corresponding values of the characteristic temperatures of θ_{D1} = 342(9), θ_{D2} = 143(3), and θ_E = 57(1). The Sommerfeld coefficient [γ = 6.8(2) mJ mol^{-1} K^{-2}] deduced from such a fit was found to perfectly agree with the value obtained above.

$$c_p T^{-3}(T) = \sum_i c_{Di} T^{-3}(T) + \sum_i c_{Ej} T^{-3}(T) + \gamma T^{-2} \quad (1)$$

$$c_{Di}(T) = 3N_{Di}R\left(\frac{T}{\Theta_{Di}}\right)^3 \int_0^{\Theta_{Di}/T} \frac{x^4 e^x}{(e^x-1)^2}\,dx \quad (2)$$

$$c_{Ej}(T) = N_{Ej}R\left(\frac{\Theta_{Ej}}{T}\right)^2 \frac{e^{\Theta_{Ej}/T}}{(e^{\Theta_{Ej}/T}-1)^2} \quad (3)$$

Obviously, the calculated number of modes as well as N_{tot} = 13 somewhat deviate from the theoretical expectations. All these results clearly evidence the complexity of the phononic spectrum of LuCuMg$_2$, which is poorly described by the simplified model given with eqn (1).

4. Conclusions

A combined study on the five {Dy, Ho, Er, Tm, Lu}CuMg$_2$ new compounds was conducted following three main lines: crystal structure, chemical bonding and magnetic properties.

These phases, existing only with heavy rare earth metals, represent a new structure type, where characteristic Mg-centred star-like clusters are condensed in 2D wavy fragments spaced by Mg slabs with a *bcc* topology. The same building principle was recognized for other $R_xCu_xMg_y$ compounds, emphasizing the correlation between their composition and the constitutive clusters' "aggregation" into the *bcc*-Mg matrix. Following this idea, the structural generalization can probably be extended to similar compounds containing different R and/or T components.

When looking at the structural peculiarities of the numerous R–T–Mg intermetallics, it becomes evident that there exist "preferred" fragments (depending on the compositional region) serving as common building moieties of the corresponding compounds. Among others, this is the case for the Mg-rich LPSO phases, featuring Mg@R_6T_8 clusters embedded in a magnesium matrix including layers of "pure" *hcp*-Mg.[21] Despite the differences in the cluster composition/geometry and in the topology of the Mg matrix, the architectures of LPSO and $R_xCu_xMg_y$ show interesting similarities, including the occurrence of pure magnesium fragments. This opens new perspectives for broadening the characterization of these two families of compounds, the former being especially studied with respect to mechanical properties and the latter with respect to

physical and magnetic behaviour. The electronic structure and bonding analyses performed on the representative $LuCuMg_2$ compound confirm its metallic character and reveal a complex bonding scenario, dominated by both hetero- and homoatomic interactions, the latter involving exclusively Mg atoms within the *bcc*-like slab. The bonding landscape is highly heterogeneous, with three distinct spatial regions identified: (i) the Mg slabs and their interface with Lu and Cu atoms, where homoatomic (among Mg species) and heteroatomic interactions coexist; (ii) the central star-like clusters composed of *fcc*-like units (8 Cu, 4 Lu, and 2 Mg), where multiatomic heteroatomic bonding occurs; and (iii) the remaining crystal space exclusively composed by Lu and Cu atoms, where heteroatomic interactions persist without Mg involvement. The negative effective charge on copper allows us to include this compound in the family of intermetallics with anionic transition metals.

The magnetic susceptibility measurements indicate that $RCuMg_2$ (R = Dy, Ho, Er, Tm) follow the Curie–Weiss law in the 20–300 K range, with effective magnetic moments almost perfectly coinciding with the theoretically calculated ones for the trivalent R-ions. The nonmagnetic $LuCuMg_2$ phonon reference compound was identified as a Pauli paramagnet. {Ho, Er, Tm}$CuMg_2$ order antiferromagnetically at critical temperatures between about 5 and 8 K, whereas $DyCuMg_2$ reveals multiple magnetic transitions. The temperature evolution of the magnetic entropy deduced from the analysis of specific heat is well below the values predicted by the classical *LS* coupling scheme, indicating the complexity of the magnetic behaviour of the studied compounds.

Conflicts of interest

There are no conflicts to declare.

Data availability

The data supporting this article have been included as part of the supplementary information (SI). Supplementary information: unit cell volume and volume contraction trends for R_2Cu_2Mg compounds; refined and optimized atomic coordinates for the studied compounds; total and atomic resolved electronic density of states calculated for {Dy, Er, Ho}$CuMg_2$; electronic band structures for ferromagnetic and antiferromagnetic {Dy, Er, Ho}$CuMg_2$. See DOI: https://doi.org/10.1039/d5dt01632k.

CCDC 2381656 ($DyCuMg_2$) contains the supplementary crystallographic data for this paper.[67]

Acknowledgements

The DynaCool-12 system was acquired within the Deutsche Forschungsgemeinschaft (DFG) Project No. 422219907.

References

1 U. C. Rodewald, B. Chevalier and R. Pöttgen, *J. Solid State Chem.*, 2007, **180**, 1720–1736.
2 P. Villars and K. Cenzual, *Pearson's Crystal Data: Crystal Structure Database for Inorganic Compounds (on DVD)*, ASM International, Materials Park, Ohio, USA, 2022/23.
3 S. Stein, L. Heletta, T. Block and R. Pöttgen, *Z. Naturforsch., B: J. Chem. Sci.*, 2018, **73**, 987–997.
4 V. V. Shtender, R. V. Denys, V. Paul-Boncour, A. B. Riabov and I. Y. Zavaliy, *J. Alloys Compd.*, 2014, **603**, 7–13.
5 X. Jiang, K. Fu, R. Xiao, Y. Wu, B. Sun, H. Shao, X. Wu, J. Zheng and X. Li, *J. Alloys Compd.*, 2018, **751**, 176–182.
6 X. Jiang, Y. Wu, K. Fu, J. Zheng and X. Li, *Intermetallics*, 2018, **95**, 73–79.
7 D. Xu, E. H. Han and Y. Xu, *Prog. Nat. Sci.: Mater. Int.*, 2016, **26**, 117–128.
8 A. H. Asadi, P. M. Kalayeh, H. Mirzadeh, M. Malekan and M. Emamy, *J. Mater. Res. Technol.*, 2023, **24**, 9513–9522.
9 S. J. B. Bin, K. S. Fong, B. W. Chua and M. Gupta, *J. Magnesium Alloys*, 2022, **10**, 899–914.
10 S. De Negri, P. Solokha, A. Saccone and V. Pavlyuk, *Intermetallics*, 2009, **17**, 614–621.
11 P. Solokha, S. De Negri, V. Pavlyuk and A. Saccone, *Intermetallics*, 2010, **18**, 719–724.
12 P. Solokha, S. De Negri, V. Pavlyuk, B. Eck, R. Dronskowski and A. Saccone, *J. Solid State Chem.*, 2010, **183**, 2995–3001.
13 P. Solokha, S. De Negri, V. Pavlyuk, A. Saccone and G. Fadda, *Eur. J. Inorg. Chem.*, 2012, **2012**, 4811–4821.
14 R. Freccero, S. De Negri, A. Saccone and P. Solokha, *Dalton Trans.*, 2020, **49**, 12056–12067.
15 P. Solokha, S. De Negri, V. Pavlyuk and A. Saccone, *Solid State Sci.*, 2009, **11**, 801–811.
16 P. Solokha, S. De Negri, V. Pavlyuk, A. Saccone and B. Marciniak, *J. Solid State Chem.*, 2007, **180**, 3066–3075.
17 M. K. Reimann, R. K. Kremer, D. Chen, R. Dronskowski, J. Kösters and R. Pöttgen, *Dalton Trans.*, 2023, **52**, 8893–8903.
18 G. Bi, H. Yan, J. Jiang, L. Tong, Y. Li, T. Chen and H. Wang, *J. Mater. Eng. Perform.*, 2025, **34**, 7244–7252.
19 M. Li, J. Kim, Z. Zhang, G. Yu, B. Jiang, T. Lee and F. Pan, *Met. Mater. Int.*, 2024, **31**, 936–944.
20 K. Guan, D. Egusa and E. Abe, *J. Magnesium Alloys*, 2022, **10**, 1573–1580.
21 P. Solokha, R. Freccero, M. Gemmi, I. Andrusenko, P. Parlanti, E. Mugnaioli, G. Steciuk, L. Palatinus and S. De Negri, *Acta Mater.*, 2025, **296**, 121279.
22 W. Hermes, S. Linsinger, S. Rayaprol, S. Tuncel, R. D. Hoffmann, R. K. Kremer, O. Jepsen and R. Pöttgen, *J. Supercond. Novel Magn.*, 2011, **24**, 1585–1592.
23 G. Kotzyba, R. Mishra and R. Pöttgen, *Z. Naturforsch., B: J. Chem. Sci.*, 2003, **58**, 497–500.
24 Bruker, *Bruker AXS Inc.:v2021.10-0*, Bruker AXS Inc., 2022.
25 Bruker, *Bruker AXS Inc.:v8.30A*, Bruker AXS Inc., 2012.
26 Bruker, *Bruker AXS Inc.:v2014/2*, Bruker AXS Inc., 2014.
27 Bruker, *Bruker AXS Inc.:v2016/2*, Bruker AXS Inc., 2016.

28 G. M. Sheldrick, *Bruker AXS Inc.:v2016/2*, Bruker AXS Inc., 2019.
29 W. Kraus and G. Nolze, *J. Appl. Crystallogr.*, 1996, **29**, 301–303.
30 D. C. Palmer, CrystalMaker Software Ltd., 2014.
31 L. Akselrud and Y. Grin, *J. Appl. Crystallogr.*, 2014, **47**, 803–805.
32 J. Rodríguez-Carvajal, Recent Developments of the Program FULLPROF, in Commission on Powder Diffraction (IUCr). Newsletter, 26, 12–19, 2001.
33 P. Blaha, K. Schwarz, F. Tran, R. Laskowski, G. K. H. Madsen and L. D. Marks, *J. Chem. Phys.*, 2020, **152**, 74101.
34 J. P. Perdew, A. Ruzsinszky, G. I. Csonka, O. A. Vydrov, G. E. Scuseria, L. A. Constantin, X. Zhou and K. Burke, *Phys. Rev. Lett.*, 2008, **100**, 136406.
35 J. P. Perdew, K. Burke and M. Ernzerhof, *Phys. Rev. Lett.*, 1996, **77**, 3865.
36 K. Koepernik and H. Eschrig, *Phys. Rev. B: Condens. Matter Mater. Phys.*, 1999, **59**, 1743.
37 F. R. Wagner and Y. Grin, *Compr. Inorg. Chem. III*, 3rd edn, 2023, vol. 1–10, pp. 222–237.
38 M. Kohout, *Int. J. Quantum Chem.*, 2004, **97**, 651–658.
39 F. R. Wagner, V. Bezugly, M. Kohout and Y. Grin, *Chem. – Eur. J.*, 2007, **13**, 5724–5741.
40 A. Ormeci, H. Rosner, F. R. Wagner, M. Kohout and Y. Grin, *J. Phys. Chem. A*, 2006, **110**, 1100–1105.
41 R. F. W. Bader, *Atoms in Molecules-A Quantum Theory*, Oxford Univ. Press, New York, 1990, p. 438.
42 M. Kohout, Program DGrid 5.0, Dresden, 2018.
43 S. Raub and G. Jansen, *Theor. Chem. Acc.*, 2001, **106**, 223–232.
44 D. Bende, F. R. Wagner and Y. Grin, *Inorg. Chem.*, 2015, **54**, 3970–3978.
45 R. Freccero, Y. Grin and F. R. Wagner, *Dalton Trans.*, 2023, **52**, 8222–8236.
46 A. Baranov, *Visualization Plugin for ParaView*, 2015.
47 R. D. Shannon, *Acta Crystallogr.*, 1976, **32**, 751–767.
48 P. Solokha, R. Freccero and S. De Negri, *J. Solid State Chem.*, 2023, **328**, 124353.
49 P. Solokha, R. Freccero and S. De Negri, *Crystallography*, 2024, **14**, 156.
50 P. Villars and J. L. C. Daams, *J. Alloys Compd.*, 1993, **197**, 177–196.
51 J. Emsley, *The elements*, Clarendon Press, 1998.
52 L. Agnarelli, Y. Prots, R. Ramlau, M. Schmidt, U. Burkhardt, A. Leithe-Jasper and Y. Grin, *Inorg. Chem.*, 2022, **61**, 16148–16155.
53 I. Antonyshyn, O. Sichevych, U. Burkhardt, A. M. Barrios Jiménez, A. Melendez-Sans, Y. F. Liao, K. D. Tsuei, D. Kasinathan, D. Takegami and A. Ormeci, *Phys. Chem. Chem. Phys.*, 2023, **25**, 31137–31145.
54 A. Martinelli, D. Ryan, J. Sereni, C. Ritter, A. Leineweber, I. Čurlík, R. Freccero and M. Giovannini, *J. Mater. Chem. C*, 2023, **11**, 7641–7653.
55 R. Freccero, P. Solokha and S. De Negri, *J. Alloys Compd.*, 2024, **995**, 174757.
56 R. Freccero, S. H. Choi, P. Solokha, S. De Negri, T. Takeuchi, S. Hirai, P. Mele and A. Saccone, *J. Alloys Compd.*, 2019, **783**, 601–607.
57 A. Amon, E. Svanidze, A. Ormeci, M. König, D. Kasinathan, D. Takegami, Y. Prots, Y. F. Liao, K. D. Tsuei, L. H. Tjeng, A. Leithe-Jasper and Y. Grin, *Angew. Chem., Int. Ed.*, 2019, **58**, 15928–15933.
58 Y. Gong, J. Wu, M. Kitano, J. Wang, T. N. Ye, J. Li, Y. Kobayashi, K. Kishida, H. Abe, Y. Niwa, H. Yang, T. Tada and H. Hosono, *Nat. Catal.*, 2018, **1**, 178–185.
59 L. Agnarelli, Y. Prots, U. Burkhardt, M. Schmidt, P. Koželj, A. Leithe-Jasper and Y. Grin, *Inorg. Chem.*, 2021, **60**, 13681–13690.
60 J. M. Hübner, W. Carrillo-Cabrera, Y. Prots, M. Bobnar, U. Schwarz and Y. Grin, *Angew. Chem., Int. Ed.*, 2019, **58**, 12914–12918.
61 U. Schwarz, R. Castillo, J. M. Hübner, A. Wosylus, Y. Prots, M. Bobnar and Y. Grin, *Z. Naturforsch., B: J. Chem. Sci.*, 2020, **75**, 209–216.
62 R. Freccero, P. Solokha, S. De Negri, A. Saccone, Y. Grin and F. R. Wagner, *Chem. – Eur. J.*, 2019, **25**, 6600–6612.
63 R. Freccero, P. Solokha, D. M. Proserpio, A. Saccone and S. De Negri, *Dalton Trans.*, 2017, **46**, 14021–14033.
64 M. K. Reimann, R. K. Kremer, D. Chen, R. Dronskowski, J. Kösters and R. Pöttgen, *Dalton Trans.*, 2023, **52**, 8893–8903.
65 E. Zuñiga-Puelles, R. Cardoso-Gil, A. Özden, N. Bulut, V. Svitlyk, C. Himcinschi, J. Kortus and R. Gumeniuk, *Phys. Rev. B*, 2022, **106**, 195201.
66 R. Gumeniuk, V. Levytskyi, B. Kundys and A. Leithe-Jasper, *Phys. Rev. B*, 2023, **108**, 214515.
67 CCDC 2381656: Experimental Crystal Structure Determination, 2025, DOI: 10.5517/ccdc.csd.cc2ky9mg.